Unraveling Rashba effect through spin-texture evolution in unidimensional-confined halide-perovskite under compression

Jagjit Kaur and Sudip Chakraborty *

Materials Theory for Energy Scavenging Lab, Harish-Chandra Research Institute, A CI of Homi Bhabha National Institute, Chhatnag Road, Jhunsi, Prayagraj 211019, India

(Received 5 September 2023; accepted 2 April 2024; published 17 May 2024)

In this work, we envisage an evolution paradigm in a promising noncentrosymmetric one-dimensional zigzag chain structure, (3AMP)BiI_5 [where AMP indicates (aminomethyl)piperidinium], through rigorous electronic structure calculations based on density functional theory (DFT). The electronic and optical properties along with the Rashba splitting and spin texture are systematically observed within the thermodynamic limit under compression equivalent to 9.6 GPa in this promising halide perovskite. Our study successfully reveals the intriguing transition of the electronic band structure from an indirect to a direct band gap phenomenon under compression in addition to an interesting redshift in the optical absorption spectra. To accurately describe the spin polarization both in plane and out of plane, we explore a three-dimensional Rashba model. The in-plane spin texture is found to arise from the octahedral distortion along the *b* direction. The fundamental interplay between structural distortions and the Rashba splitting in the considered one-dimensional system under the influence of compression along with the evolution of spin texture could hold great potential for the pursuit of sustainable energy.

DOI: 10.1103/PhysRevMaterials.8.055405

I. INTRODUCTION

Hybrid perovskites that combine organic and inorganic counterparts present an exciting opportunity to exploit the synergistic effect of both the structural units within a single structure. One particularly interesting group of materials in this context is halide hybrid perovskites, which exhibit a diverse range of magnetic, optical, and electrical phenomena resulting from the integration of organic and inorganic parts [1–3]. These materials are often characterized by networks of divalent metal halide octahedra, connected in one-, two-, or three-dimensional arrangements and interspersed with organic cations. In simplified structures of organic-inorganic hybrid systems, the organic component serves as a physical and electronic barrier, effectively insulating or encasing the lower-dimensional inorganic framework. However, in more complex hybrid perovskite systems, it involves conjugated organic molecules; the organic component actively contributes to the electronic and optical properties of the system. The presence of lower-dimensional structures in these materials gives rise to unique inherent properties, and their metal-halide-based hybrid can easily be processed at near-ambient temperatures [4–6]. As a result, organic-inorganic perovskites have garnered significant interest as potential candidates for electronic and optoelectronic devices and spintronics, offering a combination of unique properties and convenient processing capabilities [7–11].

Bismuth-based halide perovskites exhibit a propensity to form structures of multidimensional configurations. These structures include zero-dimensional compounds such as $A_3Bi_2I_9$ (where A represents Cs^+ or methylammonium), characterized by molecular dimers of $[Bi_2I_9]$ [12]. Additionally, one-dimensional (1D) chains of $A'BiI_5$ (where A' represents an organic diammonium cation) [13,14] and two-dimensional (2D) perovskites with a ⟨111⟩ orientation, denoted as $A_3Bi_2I_9$ (where A can be $(NH)^+$, K^+, or Rb^+) [15] can be observed. Alternatively, the latter can be understood as vacancy-ordered double perovskites. In these structures, a vacancy occurs in every third Bi octahedron, while the remaining two thirds of the Bi octahedra maintain connectivity via corner sharing. Maintaining corner-sharing connections is crucial to enable substantial electronic coupling and the presence of dispersive electronic bands [16]. Conversely, compounds formed by edge-sharing and face-sharing BiI_6 octahedra tend to exhibit lower-dimensional structures characterized by flat electronic bands [17].

The phenomenon of Rashba spin splitting [18] arising from the combination of spin-orbit coupling (SOC) and broken structural inversion symmetry has garnered significant interest because of its potential applications not only in spintronics but also in various optoelectronic devices [19–22]. Extensive research efforts have focused on identifying materials with pronounced Rashba spin splitting, as large band splittings are crucial for such applications. This intriguing spin splitting has been observed in diverse systems, including bulk crystals [23–28], metal surfaces [29–31], oxide and halide perovskites [32–35], semiconductor interfaces [36], quantum dots [37–39], 1D nanowires [40,41], and 1D screw dislocations in semiconductors [42–44].

The pursuit of unidimensional hybrid halide perovskites holds significant importance in the field of spin optoelectronics due to the quantum confinement effect. Moreover, such confined systems with constituent heavy elements like bismuth could be prone to the Rashba effect considering relativistic SOC and inversion symmetry breaking. The

*sudipchakraborty@hri.res.in

repercussions of Rashba splitting could be very well reflected in the charge carrier recombination rate, which is significant for manifesting efficient photovoltaic devices. One way to manipulate such a recombination rate is by tuning the Rashba splitting corresponding to the spin texture of such materials under external pressure or structural compression. The investigation of 1D $A'BiI_5$ structures was initially carried out by Mitzi and Brock [13] and Mousdis *et al.* [14] almost 30 years ago. However, the potential applications of these structures in spintronics and optoelectronics have not been explored extensively. In this study, we focus on (3AMP)BiI_5 [45], which consists of the small cyclic diammonium cation (aminomethyl)piperidinium (AMP). This compound exhibits broken inversion symmetry and strong SOC originating from the Bi and I orbitals, leading to the Rashba effect. To investigate the properties of (3AMP)BiI_5, we applied hydrostatic pressure or structural compression, which allows us to tune the Rashba splitting. This pressure-induced modification enhances the interaction between the 1D wires and leads to changes in the octahedral distortion. The interplay between the in-plane and out-of-plane orbital contributions has a significant impact on the spin texture and Rashba splitting phenomena in the material. Furthermore, the application of compression causes a redshift in the band gap of the system, making it more suitable for photovoltaic applications considering the absorption characteristics in the visible solar spectrum. By combining the advantages of its flexible structure, thermodynamic stability, strong SOC, absorption cross section in the infrared-visible (IR-vis) region, and tunable Rashba splitting, (3AMP)BiI_5 emerges as a promising candidate for various applications in optoelectronics, spintronics, and spin-orbitronics.

II. COMPUTATIONAL METHODOLOGY

First-principles electronic structure calculations based on the density functional theory (DFT) [46,47] framework, implemented in the Vienna Ab initio Simulation Package (VASP) [48], were systematically performed to determine the structural, electronic, and optical properties. The calculations employed the projector augmented wave [49] method with the Perdew-Burke-Ernzerhof (PBE) [50] exchange-correlation functional form of the generalized gradient approximation (GGA). An energy cutoff of 500 eV was used throughout all the electronic structure calculations. During the structure relaxation, ionic relaxation was performed until the total energy difference between two ionic steps was below 10^{-4} eV and the force convergence between two steps reached 10^{-5} eVÅ^{-1}. The calculations considered the effect of spin-orbit interactions throughout due to the presence of the heavy element bismuth. A Monkhorst pack scheme [51] generated $3 \times 3 \times 3$ k mesh was used, and the spin texture, represented by the expectation value of the spin operators, was extracted using the PYPROCAR program [52]. The noncollinear calculations giving spinor eigenfunctions Ψ_k and the expectation values of the spin operators S_i were obtained with $s_i = \frac{1}{2}\langle\Psi_k|\sigma_i|\Psi_k\rangle$, where σ_i represents the Pauli matrices. Both compressive and tensile compressions were thoroughly investigated through a process involving initial isotropic reduction of the unit cell volume. Subsequently, the relaxation of the unit cell shape and adjustments to the ionic positions were performed for each modified lattice constant. The following form of the third-order Birch-Murnaghan [53,54] isothermal equation was used:

$$P(V) = \frac{3B_0}{2}\left[\left(\frac{V_0}{V}\right)^{\frac{7}{3}} - \left(\frac{V_0}{V}\right)^{\frac{5}{3}}\right] \times \left\{1 + \frac{3}{4}(B_0' - 4)\left[\left(\frac{V_0}{V}\right)^{\frac{2}{3}} - 1\right]\right\},$$

where P is pressure, V_0 is the reference volume, V is the deformed volume, B_0 is the bulk modulus, and B_0' is the derivative of the bulk modulus with respect to pressure. The corresponding equation of state for the correlation between energy and volume is given by

$$E(V) = E_0 + \frac{9V_0B_0}{16}\left[\left(\frac{V_0}{V}\right)^{\frac{2}{3}} - 1\right]^3 B_0' + \frac{9V_0B_0}{16}\left[\left(\frac{V_0}{V}\right)^{\frac{2}{3}} - 1\right]^2\left[6 - 4\left(\frac{V_0}{V}\right)^{\frac{2}{3}}\right].$$

TABLE I. Formation energy.

Compression (GPa)	Formation energy (eV/unit cell)
0	−23.294
1.4	−21.314
2.5	−20.094
3.2	−19.286
6.6	−14.544
9.6	−10.174

III. RESULTS AND DISCUSSION

A. Thermodynamic stability and structural transition under compression

To determine the thermodynamic stability of a structure, the system's formation energy must be calculated. The formation energy H_f can be determined using the following equation, which takes into account the chemical potentials of bismuth, iodine, carbon, nitrogen, and hydrogen (μ_{Bi}, μ_I, μ_C, μ_N, μ_H, respectively), as well as the total energy of the system at different compression values E_{total}:

$$H_f = E_{total} - 4\mu_{Bi} - 20\mu_I - 24\mu_C - 8\mu_N - 40\mu_H. \quad (1)$$

The energies of different compounds were calculated using the PBE functional. SOC is also included for the heavy elements. At ambient pressure, the formation energy of the structure was found to be −23.294 eV per unit cell. As structural compression increases, the total energy of the system increases, resulting in a decrease in the formation energy. Table I shows that at 9.6 GPa, the formation energy is −10.174 eV per unit cell. Therefore, for further calculations, compression values ranging from 0 to 9.6 GPa will be considered because these structures are thermodynamically stable.

At ambient pressure, (3AMP)BiI_5 belongs to the monoclinic crystal system with the $P2_1$ space group. The lattice parameters after structural relaxation are found to be a =

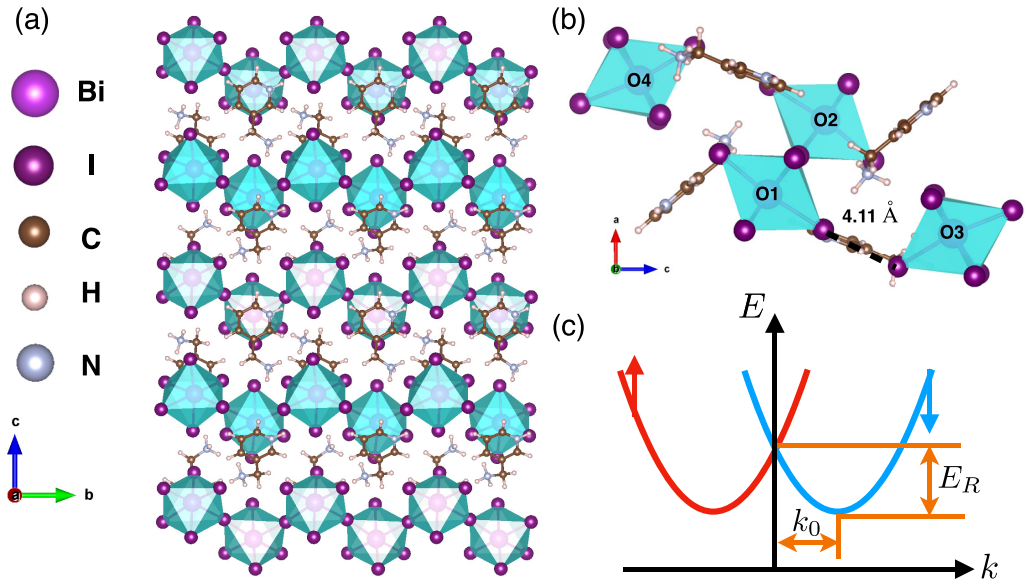

FIG. 1. (a) Side view of the crystal structure of 3AMPBiI$_5$. The stacking direction of the 1D octahedral chains is along the c axis, whereas the chain direction is along the b axis. (b) Cyan octahedra show $(BiI_6)^{3-}$. The nearest I···I distance is indicated by the dashed line. (c) Spin-polarized sub-bands (red: down spin; blue: up spin) separated in k space due to the SOC and inversion asymmetry. The energy offset E_R and momentum offset k_0 are due to Rashba splitting.

11.53 Å, $b = 9.55$ Å, and $c = 17.52$ Å, with $\alpha = 90°$. The structure, as shown in Fig. 1(a), is a 1D zigzag chain of BiI$_6$ corner-sharing octahedra. The Bi-I-Bi angle is 174.42°, and the nearest I·I distances are 4.11 Å, which is less than the sum of the van der Waals radii (4.4 Å), which suggests close interaction between the wires.

Figure 2(a) illustrates the plot of the equation of state obtained using the Birch-Murnaghan fit. The analysis of the equation of state reveals a relatively low bulk modulus of 5.62 GPa. This phenomenon can potentially be attributed to the presence of a higher proportion of flexible aliphatic (3AMP) rings within the material. Consequently, the material exhibits enhanced compressibility and elasticity. Within the detected compression range, no first-order phase transition was observed. This absence of a phase transition could potentially be attributed to the presence of highly sterically hindered aliphatic cyclic molecules within the crystal lattice.

As the structural compression increases, the system undergoes a transition from being an indirect band gap semiconductor to being a direct band gap semiconductor. Simultaneously, the nearest I · I distance consistently decreases, resulting in a stronger interaction between the wires. The lattice parameters decrease with the increase in compression, as seen in Fig. 2(b). The a and c parameters decrease the most rapidly. This may be due to the presence of a spacer cation perpendicular to the b direction. This leads to more compressibility of the a and c parameters. The bond length between Bi and I and the bond angle (I-Bi-I) exhibit alteration with increasing compression. Figures S5 and S6 in the Supplemental Material [55] depict the bond length and bond angle at 0 and 9.6 GPa, respectively. Furthermore, Figs. S7 and S8 in the Supplemental Material [55] illustrate the variations in the Bi-I-Bi bond angle at 0 and 9.6 GPa, respectively. These observations indicate a change in the angle between adjacent octahedra as structural compression increases.

In perovskite materials, the deviation of the octahedral tilt angle from 180 degrees plays a significant role in determining the material's overall properties. Let us define δ as the difference between 180° and the measured angle of Bi-I-Bi. Notably, there is a distinct variation in the response of the octahedral tilt angle deviation for different octahedra.

For Bi(1)-I(7/8)-Bi(2), δ initially decreases until it reaches 1.4 GPa, after which it starts to increase, as seen in Fig. 2(c). Conversely, for Bi(3)-I(17/18)-Bi(4), the opposite trend is observed. As structural compression increases, δ generally increases for all compression points, except at 3.2 GPa, where a slight dip is observed specifically for Bi(3)-I(18)-Bi(4).

Figure 1(b) reveals the formation of four octahedra, each centered around a Bi atom. The adjacent chains of octahedra also exhibit rotation, resulting in distinct compression responses for each octahedron. To quantify the distortion, we calculate the distortion index D using the equation $D = \frac{1}{6}\sum_i^6 \frac{|l_i - l_{av}|}{l_{av}}$. Here, l_i represents the individual Bi-I bond lengths, while l_{av} denotes the average bond length. Let us denote the octahedra corresponding to Bi1, Bi2, Bi3, and Bi4 as O1, O2, O3, and O4, respectively.

Interestingly, for O1 and O2, the distortion index decreases with increasing compression, as seen in Fig. 3 and Table S1. However, for O3 and O4, the distortion index initially decreases and then begins to increase. This indicates that beyond a certain compression threshold, the octahedra deviate from their regular octahedral coordination with iodine, making iodide double perovskites quite rare. The anisotropic variation in octahedral distortion is likely influenced by the absence of inversion symmetry and the presence of easily deformable organic layers (3AMP). The degree of octahedral distortion is more localized specifically in our crystal structure, i.e., a one-dimensional chain of (3AMP)BiI$_5$, which from the macroscopic perspective does not really impact the global phase transition of the corresponding structural

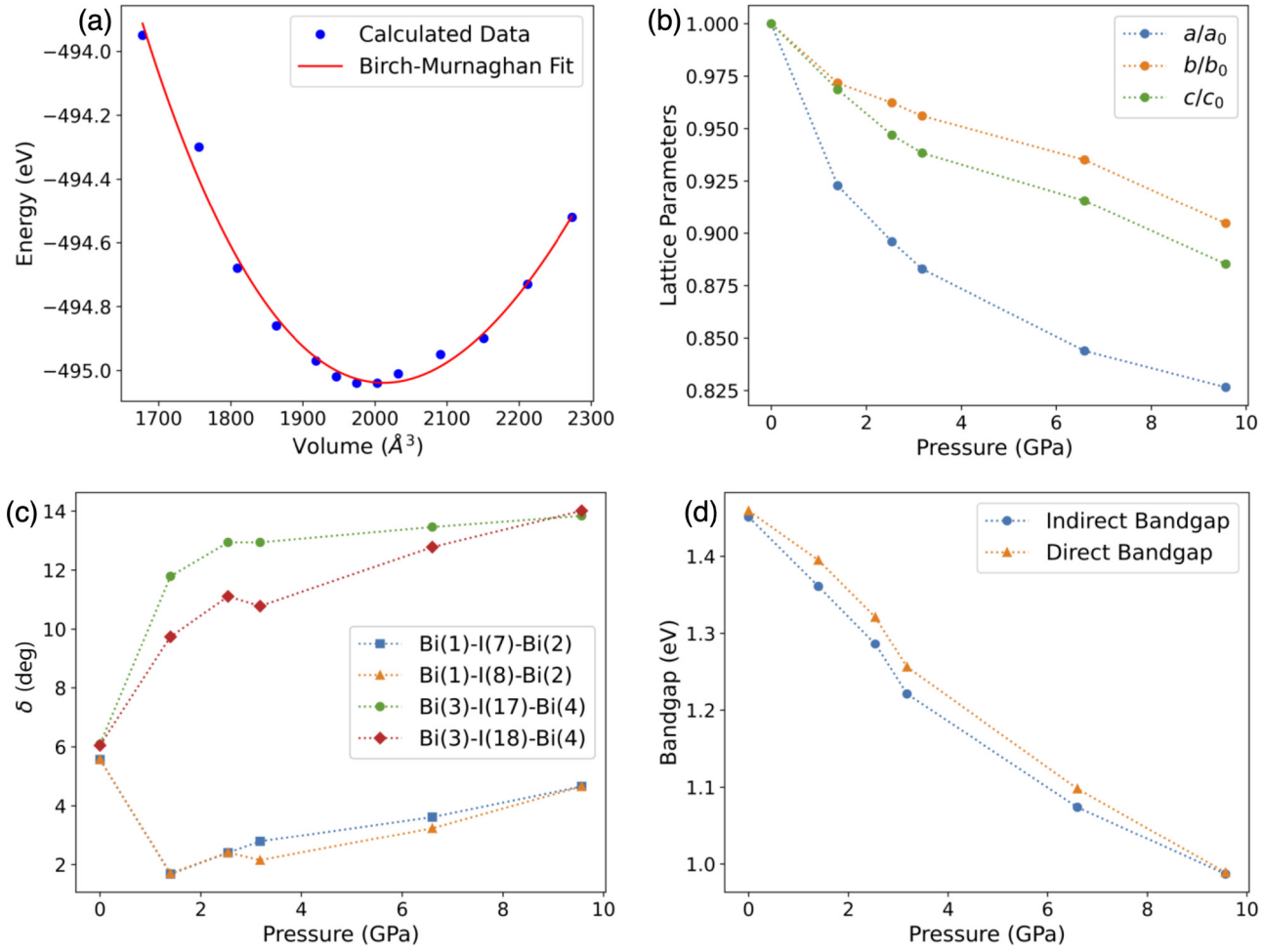

FIG. 2. (a) Equation of state using the Birch-Murnaghan fit to give the correlation between the energy and volume using Eq. (1). (b) Evolution of the lattice parameters with structural compression. (c) Evolution of the octahedral tilt angle δ with pressure. δ is defined as the difference between 180° and the measured angle of Bi-I-Bi. (d) Evolution of the band gap with structural compression.

configuration. However, it does lead to a change in the corresponding Rashba band splitting, as evidenced by variations in the Rashba parameter. This is because the local octahedral distortion impacts the individual Bi-I bond length and bond angles I-Bi-I, which has a corresponding repercussion on the electronic band structure as the organic counterpart of (3AMP)BiI_5 does not contribute strongly to the electronic structure. However, it does lead to changes in the Rashba effect, as evidenced by variations in the Rashba parameter. A similar observation was found in an earlier study [56], highlighting the role of octahedral rotation, rather than *M*-*X* bond contraction, in driving phase transitions.

B. Electronic structure evolution under compression

At ambient pressure, the indirect and direct band gaps of the material using the PBE functional including SOC are determined to be 1.45 and 1.46 eV, respectively, which is in reasonable agreement with the reported value [45]. The valence band maximum (VBM) is located at the Γ high-symmetry point, while the conduction band minimum (CBM) is found at the *A* high-symmetry point. The Brillouin zone with high-symmetry points is represented in Fig. S2 in the Supplemental Material [55]. As the structural compression increases, the band gap values decrease, and the band gap nature transforms from indirect to direct. At 9.6 GPa, the band gap reduces to 0.99 eV, exhibiting a redshift. At 2.5 GPa, the indirect band gap becomes 1.29 eV, while the direct band gap becomes 1.3 eV. This configuration is particularly suitable for photovoltaic applications. Additionally, Rashba-type band splitting occurs at both the VBM and CBM, with a more pronounced effect observed at the Γ point in the VBM. The rate at which the band gap decreases is measured to be 0.048 eV G^{-1}Pa. The lattice compression causing this reduction may be attributed to the low bulk modulus of the system.

The band structure analysis (Fig. 4) reveals distinct characteristics of the valence and conduction bands. The valence bands exhibit relatively flat behavior, while the conduction bands display greater dispersion. Examining the partial density of states, it becomes evident that the valence band edge primarily consists of I 5*p* orbitals, whereas the conduction band edge arises from a hybridization of Bi 6*p* and I 5*p* orbitals.

At ambient pressure, the bands demonstrate enhanced dispersion along the $(BiI_6)^{3-}$ chain direction due to the presence of corner-sharing octahedra in the real-space

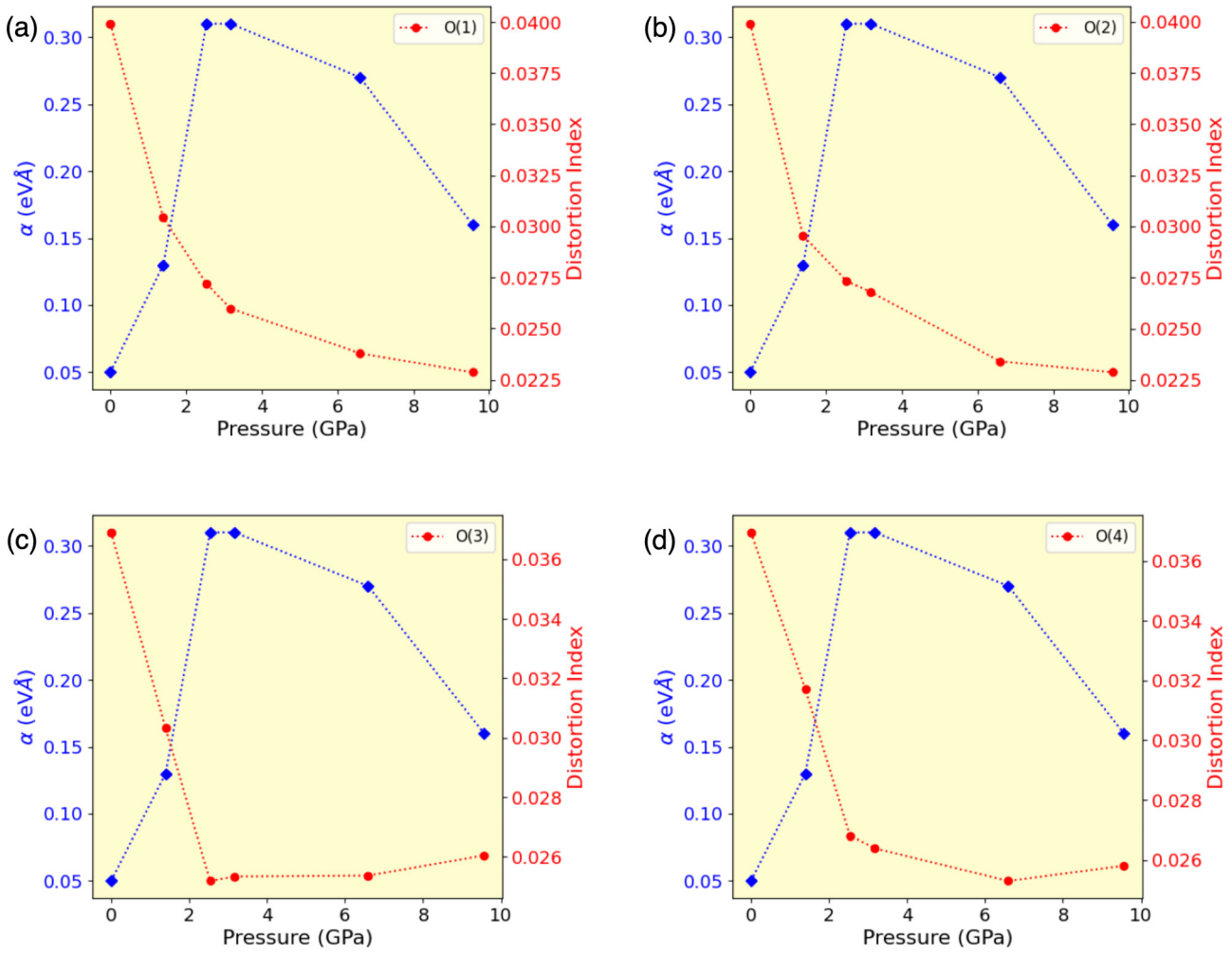

FIG. 3. Evolution of the octahedral distortion index D and Rashba splitting values α_R with structural compression. The octahedral distortion index is calculated using the equation $D = \frac{1}{6}\sum_i^6 \frac{|l_i - l_{av}|}{l_{av}}$. Here, l_i represents the individual Bi-I bond lengths, while l_{av} denotes the average bond length. The Rashba splitting α_R is defined by $\alpha_R = 2E_R/k_0$.

structure. In other directions, the bands exhibit slight dispersion, influenced by the I · I interactions between the wires. As compression increases, the distance between I · I decreases, intensifying the interaction between the wires and resulting in more dispersive valence bands. Starting from 3.2 GPa, the I $5p$ orbitals begin to contribute significantly near the Fermi level, leading to further dispersion in the valence bands at 9.6 GPa. Additionally, the influence of the organic compounds becomes more pronounced in the valence band region as the structural compression increases. This indicates that the flexible 3AMP rings within the organic part start to impact the electronic structure at higher compression values.

C. Structural compression induced optical absorption spectra evolution

The optical absorption spectra were determined by calculating the frequency-dependent dielectric function, denoted as $\varepsilon(\omega) = \varepsilon_1(\omega) + i\varepsilon_2(\omega)$ [57]. The absorption coefficient is dependent on both the imaginary and real parts of the dielectric function obtained through the first-principles DFT PBE functional including SOC. Applying Fermi's golden rule, we can derive the imaginary part of the dielectric function, which involves the summation of occupied and unoccupied states:

$$\varepsilon_2(\omega) = \frac{4\pi^2 e^2}{\Omega} \lim_{q\to 0} \frac{1}{q^2} \sum_{c,v,k} 2\omega_k \delta(\varepsilon_{ck} - \varepsilon_{vk} - \omega) \times \langle \nu_{ck+e_\alpha q} | \nu_{vk} \rangle \langle \nu_{ck+e_\beta q} | \nu_{vk} \rangle^*. \quad (2)$$

Here, q represents the propagating wave vector, and ω denotes the frequency. ν_{ck} and ν_{vk} denote the crystal wave functions at specific points in the conduction band and valence band, respectively. The indices c and v refer to the conduction band and valence band, respectively. Employing the Kramers-Kronig relation, we can obtain the real part of the dielectric function. By utilizing the obtained real and imaginary parts of the dielectric function, we obtain the absorption cross section as a function of photon energy using the following equation:

$$\alpha(\omega) = \frac{2\omega}{c} \left[\frac{\sqrt{\varepsilon_1^2 + \varepsilon_2^2} - \varepsilon_1}{2} \right]^{\frac{1}{2}}. \quad (3)$$

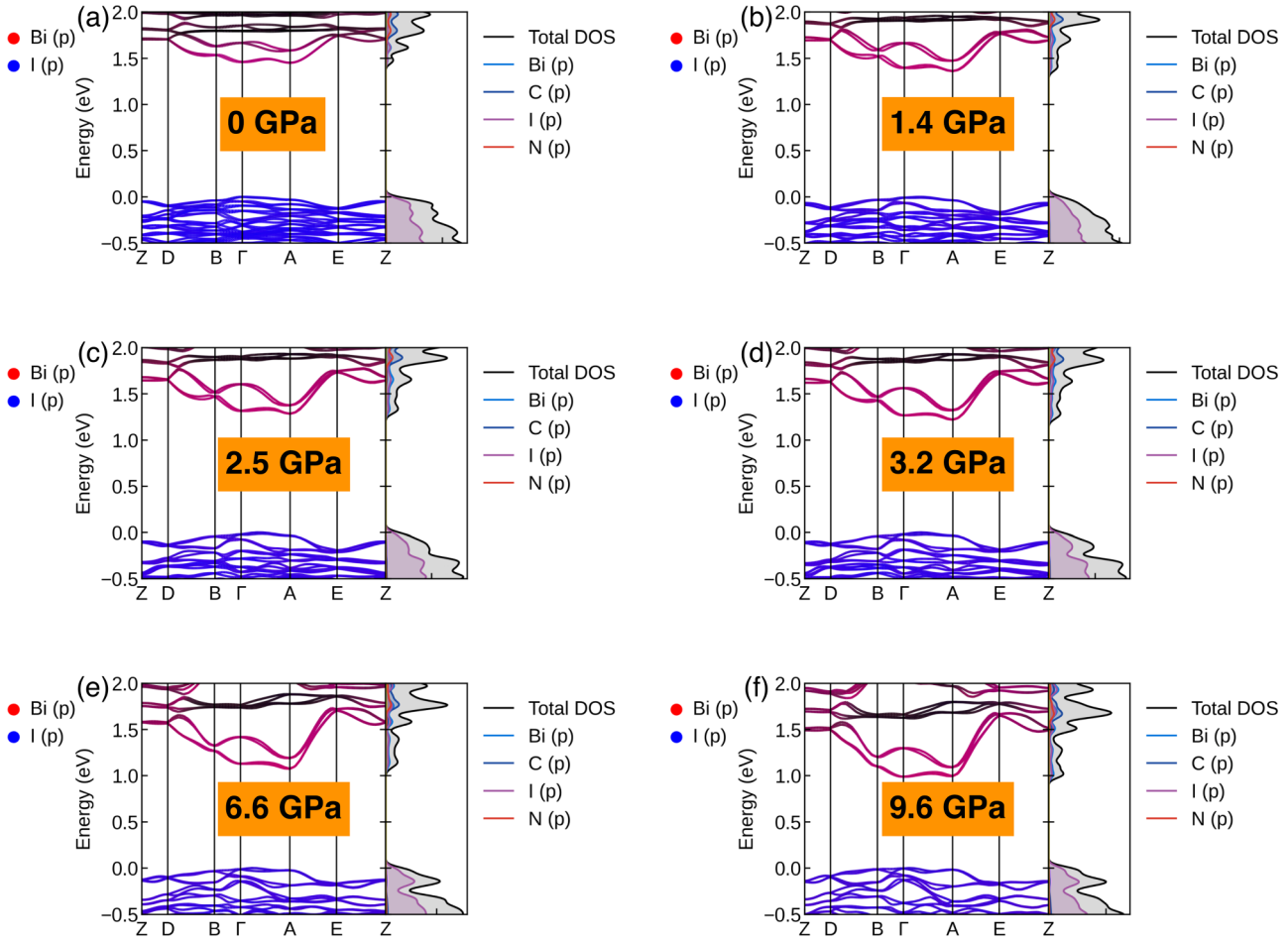

FIG. 4. Evolution of the electronic structure with compression. (a) Ambient pressure, (b) 1.4 GPa, (c) 2.5 GPa, (d) 3.2 GPa, (e) 6.6 GPa, and (f) 9.6 GPa. The valence band maximum (VBM) is located at the Γ high-symmetry point, while the conduction band minimum (CBM) is found at the *A* high-symmetry point. With the increase in the pressure, band gap decreases, and the valence bands become more dispersive. Atom-projected band structures show the valence band edge is made up of I 5*p* orbitals and the conduction band edge arises from a hybridization of Bi 6*p* and I 5*p* orbitals.

In Eq. (3), $\alpha(\omega)$ represents the absorption cross section at a given photon energy ω, c denotes the speed of light, and ε_1 and ε_2 are the real and imaginary parts of the dielectric function, respectively.

One-dimensional perovskites, with their unique zigzag chains and lower dimensionality, hold great potential for photovoltaic applications. The optical band gap, which represents the starting point of the absorption spectra at ambient pressure, is measured to be 1.4 eV, corresponding to the IR region of the electromagnetic radiation (Fig. 5). Notably, the peak of the absorption spectra occurs at 2.5 eV, falling within the visible region. Given that the solar flux exhibits maximum intensity in the IR and visible range, (3AMP)BiI_5 emerges as a promising candidate for solar cell applications. Furthermore, when subjected to structural compression, the optical band gap experiences a decrease and undergoes a redshift. This can be observed in Fig. 5, where both the onset and peak of the spectra shift towards lower energy. Consequently, compression results in a reduction of the band gap and a redshift in the absorption spectra. This indicates that 1D perovskites are increasingly well suited for solar

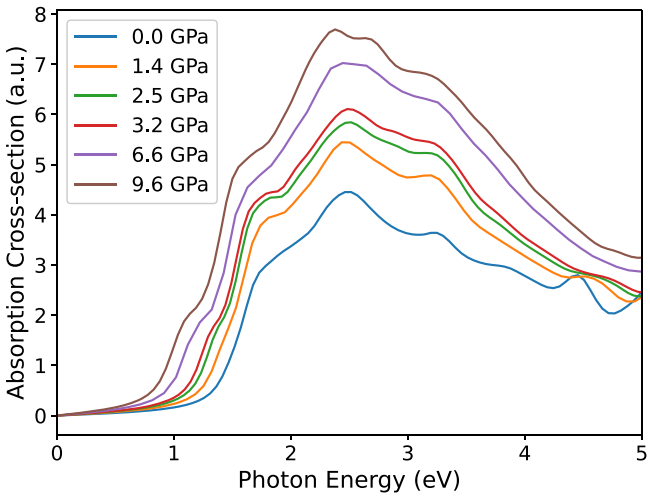

FIG. 5. Evolution of absorption optical spectra under compression. Subject to structural compression, the optical band gap experiences a decrease and undergoes a redshift.

TABLE II. Evolution of Rashba splitting values with respect to structural compression.

Pressure (GPa)	Rashba energy E_R (meV)		Momentum offset k_0 (10^{-3} Å^{-1})		Rashba splitting α_R (eVÅ)	
	$\Gamma \to A$	$\Gamma \to B$	$\Gamma \to A$	$\Gamma \to B$	$\Gamma \to A$	$\Gamma \to B$
0	0.6	0.4	25.04	9.20	0.05	0.09
1.4	7.0	0.8	106.2	14.2	0.13	0.11
2.5	19.9	0.8	127.0	14.6	0.31	0.11
3.2	18.8	0.8	119.5	14.7	0.31	0.11
6.6	13.0	1.7	96.0	20.3	0.27	0.17
9.6	3.1	1.1	39.3	20.7	0.16	0.11

cell applications under compression, making them highly desirable.

D. Repercussion of compression on Rashba splitting and spin texture

The presence of I $5p$ orbitals in the VBM introduces strong spin-orbit coupling, which lifts the spin degeneracy and splits the band into two at the Γ point. This spin splitting leads to anisotropic band dispersion, with distinct splitting patterns along the $\Gamma \to A$ and $\Gamma \to B$ directions (Fig. S4 in the Supplemental Material [55]). The corresponding Rashba energy E_R, momentum offset k_0, and Rashba splitting α_R are summarized in Table II. The Rashba splitting α_R is defined by $\alpha_R = 2E_R/k_0$. It is noteworthy that the α_R value along the $\Gamma \to A$ direction exhibits greater sensitivity to structural compression. Initially, it increases with increasing compression, reaching a maximum value of 0.31 eVÅ at 3.2 GPa before starting to decrease. This behavior can be correlated with the trend observed in the octahedral distortion, as illustrated in Fig. 3. The similarity in the trends suggests a potential connection between the octahedral distortion and the variation of the Rashba splitting α_R under compression.

In order to investigate the Rashba splitting in the $\Gamma \to A$ direction, we performed calculations to determine the spin texture in the k_x-k_z plane. Figures 6 and 7 present the 2D contour plots of constant energy, illustrating the spin texture calculated in a k_x-k_z plane centered at the Γ point. Notably, the plots clearly demonstrate the Rashba-type spin splitting of the electronic bands into spin-up (red) and spin-down (blue) states. At ambient pressure (Fig. 6, top row), the spin polarization in the S_x (in-plane) and S_z (out-of-plane) directions exhibits Rashba-type splitting. However, the in-plane S_y component is absent. The presence of Rashba band splitting in the k_x-k_z direction may be attributed to the presence of aliphatic rings within the a-c plane, leading to a breaking of the system's symmetry. As the compression increases, the contribution of the in-plane S_y component starts to exhibit Rashba-like splitting as well. This observation suggests that the octahedral distortion of O3 and O4 (along the b direction), which intensifies under structural compression, enhances the in-plane Rashba spin texture.

The traditional 2D Rashba model, given by $H_R^{2D} = \alpha_R^{2D}(\mathbf{k} \times \hat{z}) \cdot \boldsymbol{\sigma} = \alpha_R^{2D}(k_y\sigma_x - k_x\sigma_y)$, where α_R^{2D} is the 2D Rashba coefficient, $\boldsymbol{\sigma} = (\sigma_x, \sigma_y, \sigma_z)$ is the Pauli matrix, $\mathbf{k} =$

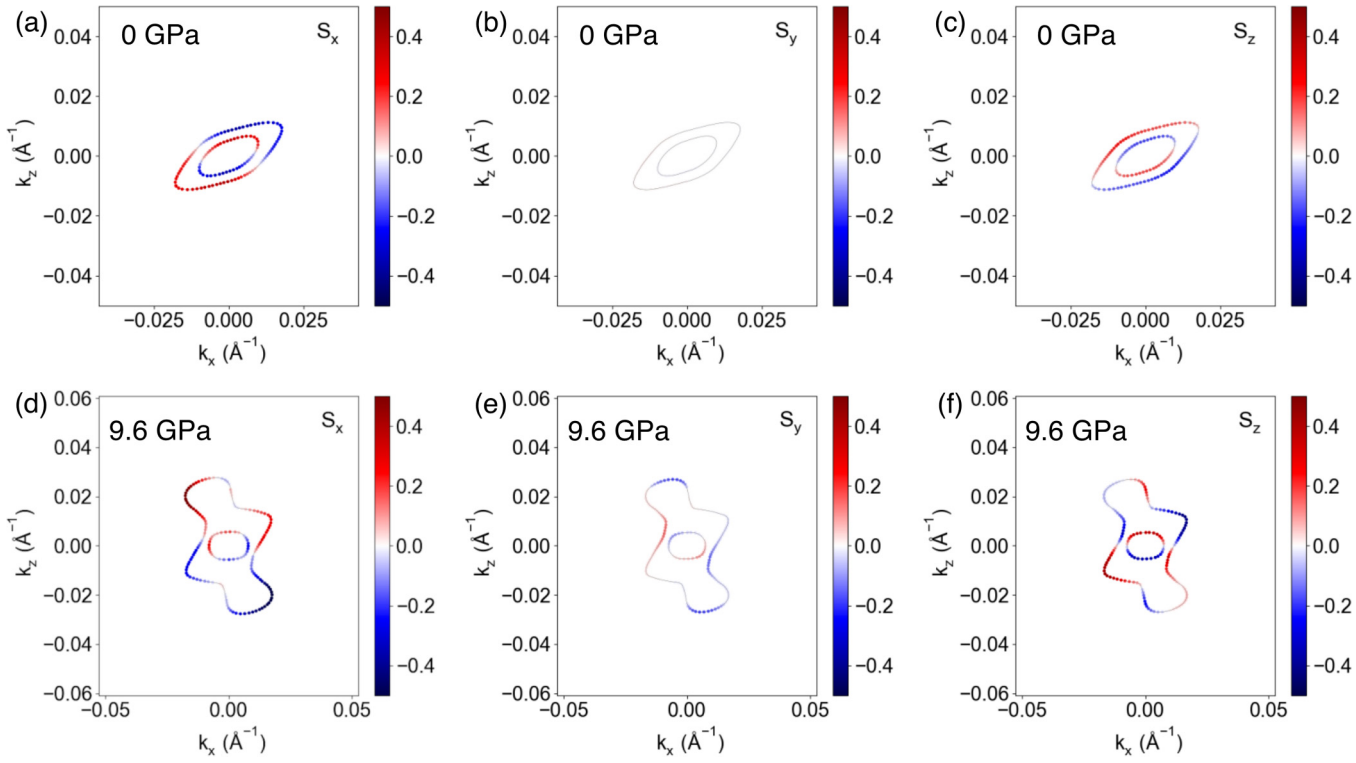

FIG. 6. Evolution of spin texture with structural compression. (a)–(c) The spin texture at ambient pressure along the S_x, S_y, and S_z directions, respectively. The spin textures are calculated at constant energy $E = E_F - 0.298$ eV. (d)–(f) The spin texture at 9.6 GPa along the S_x, S_y, and S_z directions, respectively. The spin textures are calculated at constant energy $E = E_F - 0.337$ eV.

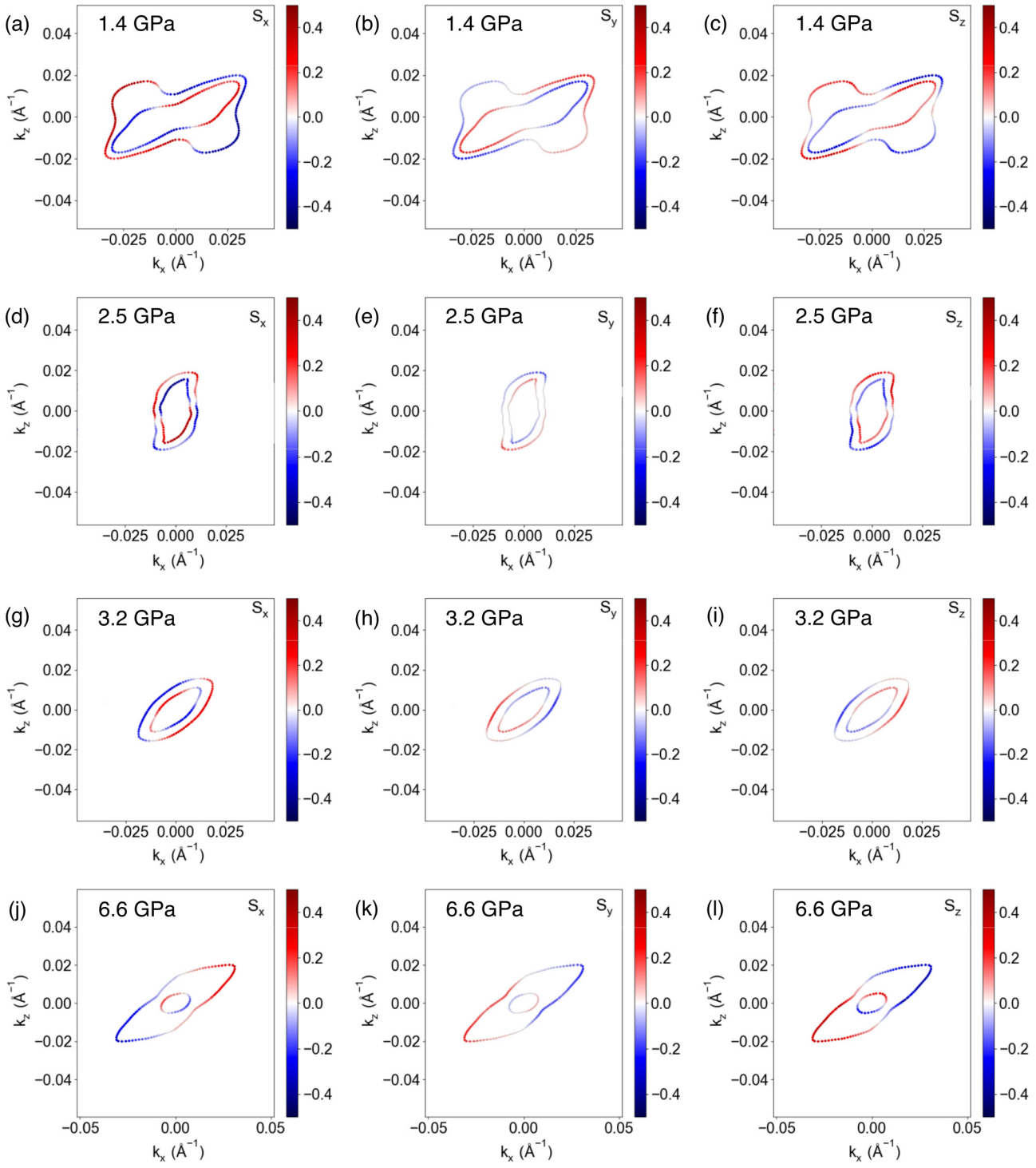

FIG. 7. Evolution of spin texture with structural compression. The first, second, and third columns denote the S_x, S_y, and S_z directions, respectively. (a)–(c) Spin texture at 1.4 GPa and constant energy $E = E_F - 0.315$ eV. (d)–(f) Spin texture at 2.5 GPa and constant energy $E = E_F - 0.325$ eV. (g)–(i) Spin texture at 3.2 GPa and constant energy $E = E_F - 0.488$ eV. (j)–(l) Spin texture at 6.6 GPa and constant energy $E = E_F - 0.310$ eV.

(k_x, k_y, k_z) is the wave vector, and $\hat{z}$ represents the out-of-plane direction, cannot fully describe the observed phenomena since both in-plane and out-of-plane splittings are present. The anisotropic Rashba effect has the potential to influence spin textures by generating out-of-plane spin textures. Upon the application of hydrostatic pressure, the spin texture begins to evolve in out-of-plane directions [58]. This evolution is attributed to local symmetry breaking caused by octahedral distortion, which may lead to the development of local polarization fields [59], extending beyond the typical Rashba length scale of 1–2 nm [60]. The presence of the out-of-plane splitting suggests that the traditional 2D Rashba model may not

be adequate to describe our results. Therefore, a 3D Rashba model was introduced to describe the observed phenomena.

Based on the Hamiltonian of the SOC, the 3D Rashba Hamiltonian [26] can be described as

$$H_R^{3D} = \frac{\alpha_0 e\hbar}{4m_0^2c^2}[\nabla \mathbf{V} \times \mathbf{P}] \cdot \boldsymbol{\sigma} = \frac{\alpha_0 e\hbar^2}{4m_0^2c^2}[\mathbf{k} \times \mathbf{E}] \cdot \boldsymbol{\sigma}. \quad (4)$$

Here, α_0 is the Rashba primary correlation factor, $\mathbf{E} = (E_x, E_y, E_z) = -\nabla \mathbf{V}$ represents the 3D electric field, and the relationship $\mathbf{P} = \hbar\mathbf{k}$ is used.

Furthermore,

$$\begin{aligned} H_R^{3D} = {} & \frac{2}{\hbar} S_x[\alpha_R(E_z)k_y - \alpha_R(E_y)k_z] \\ & + \frac{2}{\hbar} S_y[\alpha_R(E_x)k_z - \alpha_R(E_z)k_x] \\ & + \frac{2}{\hbar} S_z[\alpha_R(E_y)k_x - \alpha_R(E_x)k_y], \end{aligned} \quad (5)$$

where $\alpha_R(E_j) = \frac{\alpha_0 e\hbar^2}{4m_0^2c^2}E_j$ (where $j = x, y, z$) is defined as the 3D Rashba coefficient, which depends on the electric field and $\mathbf{S} = (S_x, S_y, S_z) = \frac{\hbar}{2}(\sigma_x, \sigma_y, \sigma_z)$ is the spin operator.

Based on the aforementioned 3D Rashba model, the orbital contribution in the k_x (k_z) direction will involve either p_z or p_y orbitals (p_x or p_y orbitals) or a combination of both. This implies that the potential gradient will be present in the z or y direction (x or y direction) or both. Analyzing the orbital-decomposed density of states (Fig. S1 in the Supplemental Material [55]), we observe that in the pristine state, there is a significantly smaller contribution from the p_y orbital in the VBM near the Fermi level. However, as structural compression increases, the p_y orbital begins to contribute, which can be attributed to the octahedral distortion. Consequently, this leads to the presence of spin texture in all three spin components, as depicted in Fig. 7, in contrast to the structure observed at ambient pressure. Notably, the out-of-plane component S_z also exhibits a nonzero spin texture due to the close proximity of the I · I interactions, resulting in stronger wire-to-wire interactions and enhanced overlap of the I $5p$ orbitals. Given that the Rashba splitting takes place within the three-dimensional space, distinct potential gradients in different directions can lead to differing levels of splitting. This phenomenon results in the observed anisotropic splitting effect.

IV. CONCLUSION

In summary, our first-principles DFT study successfully demonstrated that the electronic, optical, and Rashba splittings of the 1D system can be effectively tuned by applying structural compression. We observed that the system remains thermodynamically stable up to 9.6 GPa, exhibiting a negative formation energy. The flexibility of the 1D structure, attributed to the presence of bendable aliphatic (3AMP) rings, is supported by a bulk modulus of 5.62 GPa. Under compression, the system undergoes an indirect to direct band gap transition, while the distortion index of the octahedra decreases. The optical absorption spectra also show a redshift with increasing compression, shifting the peak towards the IR-vis region. The Rashba effect, resulting from the splitting of the VBM at the Γ point, was clearly observed, and its sensitivity to hydrostatic compression is evident from the anisotropic band splitting along the $\Gamma \rightarrow A$ and $\Gamma \rightarrow B$ directions. Notably, the α_R splitting exhibited a more prominent effect along the $\Gamma \rightarrow A$ direction, as confirmed by the spin-texture calculations in the k_x-k_z plane. To explain these results, we employed a three-dimensional Rashba model accounting for the presence of out-of-plane spin texture. Furthermore, we found that the contribution of the I p_y orbital in the VBM increased with increasing compression. The anisotropic Rashba splitting and the presence of the out-of-plane spin texture could be rigorously tuned through structural compression due to the flexibility provided by the 3AMP rings and the enhanced octahedral distortion. Overall, these unique findings position the 1D zigzag perovskite chain of (3AMP)BiI_5 as an emerging and promising candidate for bifunctional applications in optoelectronics and spintronics because their electronic, optical, and Rashba splittings can be effectively controlled through structural compression. This particular investigation of Rashba splitting evolution (using PBE-GGA + SOC) under structural compression in unidimensional confined halide hybrid perovskite could certainly pave the way for future strategies of fine-tuning the charge carrier recombination, the fundamental mechanism behind the efficiency in optoelectronic applications like solar cells and light-emitting diodes in addition to spin-orbitronics.

ACKNOWLEDGMENTS

The authors would like to acknowledge HRI for infrastructure and high-performance computing facilities.

[1] D. B. Mitzi, C. A. Feild, W. T. A. Harrison, and A. M. Guloy, Conducting tin halides with a layered organic-based perovskite structure, Nature (London) **369**, 467 (1994).

[2] D. B. Mitzi, S. Wang, C. A. Feild, C. A. Chess, and A. M. Guloy, Conducting layered organic-inorganic halides containing-oriented perovskite sheets, Science **267**, 1473 (1995).

[3] A. Kojima, K. Teshima, Y. Shirai, and T. Miyasaka, Organometal halide perovskites as visible-light sensitizers for photovoltaic cells, J. Am. Chem. Soc. **131**, 6050 (2009).

[4] K. R. Hansen, C. E. McClure, J. S. Colton, and L. Whittaker-Brooks, Franz-Keldysh and Stark effects in two-dimensional metal halide perovskites, PRX Energy **1**, 013001 (2022).

[5] H. Lu, G. Koknat, Y. Yao, J. Hao, X. Qin, C. Xiao, R. Song, F. Merz, M. Rampp, S. Kokott, C. Carbogno, T. Li, G. Teeter, M. Scheffler, J. J. Berry, D. B. Mitzi, J. L. Blackburn, V. Blum, and M. C. Beard, Electronic impurity doping of a 2D hybrid lead iodide perovskite by Bi and Sn, PRX Energy **2**, 023010 (2023).

[6] N. J. Weadock, C. MacKeen, X. Qin, L. Waquier, Y. Rakita, J. A. Vigil, H. I. Karunadasa, V. Blum, M. F. Toney, and F. Bridges, Thermal contributions to the local and long-range structural disorder in $CH_3NH_3PbBr_3$, PRX Energy **2**, 033004 (2023).

[7] D. B. Mitzi, K. Chondroudis, and C. R. Kagan, Organic-inorganic electronics, IBM J. Res. Dev. **45**, 29 (2001).

[8] K. Chondroudis and D. B. Mitzi, Electroluminescence from an organicinorganic perovskite incorporating a quaterthiophene dye within lead halide perovskite layers, Chem. Mater. **11**, 3028 (1999).

[9] M. Era, S. Morimoto, T. Tsutsui, and S. Saito, Organic–inorganic heterostructure electroluminescent device using a layered perovskite semiconductor $(C_6H_5C_2H_4NH_3)_2PbI_4$, Appl. Phys. Lett. **65**, 676 (1994).

[10] A. K. Jena, A. Kulkarni, and T. Miyasaka, Halide perovskite photovoltaics: Background, status, and future prospects, Chem. Rev. **119**, 3036 (2019).

[11] L. Yu and A. Zunger, Identification of potential photovoltaic absorbers based on first-principles spectroscopic screening of materials, Phys. Rev. Lett. **108**, 068701 (2012).

[12] K. McCall, C. Stoumpos, S. Kostina, M. Kanatzidis, and B. Wessels, Strong electron-phonon coupling and self-trapped excitons in the defect halide perovskites $A_3M_2I_9$ (A = Cs, Rb; M = Bi, Sb), Chem. Mater. **29**, 4129 (2017).

[13] D. B. Mitzi and P. Brock, Structure and optical properties of several organic-inorganic hybrids containing corner-sharing chains of bismuth iodide octahedra, Inorg. Chem. **40**, 2096 (2001).

[14] G. A. Mousdis, G. C. Papavassiliou, A. Terzis, and C. P. Raptopoulou, Notizen: Preparation, structures and optical properties of $[H_3N(CH_2)_6NH_3]BiX_5$ (X=I, Cl) and $[H_3N(CH_2)_6NH_3]SbX_5$ (X=I, Br), Z. Naturforsch. B **53**, 927 (1998).

[15] A. J. Lehner, D. H. Fabini, H. A. Evans, C.-A. Hébert, S. R. Smock, J. Hu, H. Wang, J. W. Zwanziger, M. L. Chabinyc, and R. Seshadri, Crystal and electronic structures of complex bismuth iodides $A_3Bi_2I_9$ (A = K, Rb, Cs) related to perovskite: Aiding the rational design of photovoltaics, Chem. Mater. **27**, 7137 (2015).

[16] X. Li, Y. He, M. Kepenekian, P. Guo, W. Ke, J. Even, C. Katan, C. C. Stoumpos, R. D. Schaller, and M. G. Kanatzidis, Three-dimensional lead iodide perovskitoid hybrids with high x-ray photoresponse, J. Am. Chem. Soc. **142**, 6625 (2020).

[17] N. Mercier, N. Louvain, and W. Bi, Structural diversity and retro-crystal engineering analysis of iodometalate hybrids, CrystEngComm **11**, 720 (2009).

[18] Y. A. Bychkov and E. I. Rashba, Oscillatory effects and the magnetic susceptibility of carriers in inversion layers, J. Phys. C **17**, 6039 (1984).

[19] S. Datta and B. Das, Electronic analog of the electro–optic modulator, Appl. Phys. Lett. **56**, 665 (1990).

[20] E. I. Rashba, Spintronics: Sources and challenge. Personal perspective, J. Supercond. **15**, 13 (2002).

[21] A. Manchon, H. C. Koo, J. Nitta, S. M. Frolov, and R. A. Duine, New perspectives for Rashba spin-orbit coupling, Nat. Mater. **14**, 871 (2015).

[22] M. Kepenekian, R. Robles, C. Katan, D. Sapori, L. Pedesseau, and J. Even, Rashba and Dresselhaus effects in hybrid organic–inorganic perovskites: From basics to devices, ACS Nano **9**, 11557 (2015).

[23] K. Ishizaka, M. S. Bahramy, H. Murakawa, M. Sakano, T. Shimojima, T. Sonobe, K. Koizumi, S. Shin, H. Miyahara, A. Kimura *et al.*, Giant Rashba-type spin splitting in bulk BiTeI, Nat. Mater. **10**, 521 (2011).

[24] J. Kaur and S. Chakraborty, Tuning spin texture and spectroscopic limited maximum efficiency through chemical composition space in double halide perovskites, ACS Appl. Energy Mater. **5**, 5579 (2022).

[25] S. Chakraborty and M. K. Nazeeruddin, The status quo of Rashba phenomena in organic–inorganic hybrid perovskites, J. Phys. Chem. Lett. **12**, 361 (2021).

[26] R. Xie, P. Cao, Z. Xu, B. Xu, J. Fu, X. Zhu, X. Fu, S.-Y. Xie, Y. Jiang, and A. Pan, Three-dimensional Rashba spin splitting dominated by out-of-plane spin polarization, Phys. Rev. B **107**, 155436 (2023).

[27] B. Monserrat and D. Vanderbilt, Temperature dependence of the bulk Rashba splitting in the bismuth tellurohalides, Phys. Rev. Mater. **1**, 054201 (2017).

[28] Z. Wang, J.-W. Luo, and A. Zunger, Alloy theory with atomic resolution for Rashba or topological systems, Phys. Rev. Mater. **3**, 044605 (2019).

[29] S. LaShell, B. A. McDougall, and E. Jensen, Spin splitting of an Au(111) surface state band observed with angle resolved photoelectron spectroscopy, Phys. Rev. Lett. **77**, 3419 (1996).

[30] Y. M. Koroteev, G. Bihlmayer, J. E. Gayone, E. V. Chulkov, S. Blügel, P. M. Echenique, and P. Hofmann, Strong spin-orbit splitting on Bi surfaces, Phys. Rev. Lett. **93**, 046403 (2004).

[31] K. Sugawara, T. Sato, S. Souma, T. Takahashi, M. Arai, and T. Sasaki, Fermi surface and anisotropic spin-orbit coupling of Sb(111) studied by angle-resolved photoemission spectroscopy, Phys. Rev. Lett. **96**, 046411 (2006).

[32] S. Sheoran, M. Kumar, P. Bhumla, and S. Bhattacharya, Rashba spin splitting and anomalous spin textures in the bulk ferroelectric oxide perovskite KIO_3, Mater. Adv. **3**, 4170 (2022).

[33] M. Gupta and B. R. K. Nanda, Spin texture as polarization fingerprint of halide perovskites, Phys. Rev. B **105**, 035129 (2022).

[34] P. Bhumla, D. Gill, S. Sheoran, and S. Bhattacharya, Origin of Rashba spin splitting and strain tunability in ferroelectric bulk $CsPbF_3$, J. Phys. Chem. Lett. **12**, 9539 (2021).

[35] A. C. Garcia-Castro, M. G. Vergniory, E. Bousquet, and A. H. Romero, Spin texture induced by oxygen vacancies in strontium perovskite (001) surfaces: A theoretical comparison between $SrTiO_3$ and $SrHfO_3$, Phys. Rev. B **93**, 045405 (2016).

[36] J. Nitta, T. Akazaki, H. Takayanagi, and T. Enoki, Gate control of spin-orbit interaction in an inverted $In_{0.53}Ga_{0.47}As/In_{0.52}Al_{0.48}As$ heterostructure, Phys. Rev. Lett. **78**, 1335 (1997).

[37] V. Fritsch, J. D. Thompson, and J. L. Sarrao, Spin and orbital frustration in $R InCu_4$ (R = Gd, Dy, Ho, and Er), Phys. Rev. B **71**, 132401 (2005).

[38] A. Varykhalov, J. Sánchez-Barriga, A. M. Shikin, W. Gudat, W. Eberhardt, and O. Rader, Quantum cavity for spin due to spin-orbit interaction at a metal boundary, Phys. Rev. Lett. **101**, 256601 (2008).

[39] N. Tripathy and A. D. Sarkar, Anisotropy in colossal piezoelectricity, giant Rashba effect and ultrahigh carrier mobility in Janus structures of quintuple Bi_2X_3 (X = S, Se) monolayers, J. Phys.: Condens. Matter **35**, 335301 (2023).

[40] M. Governale and U. Zülicke, Spin accumulation in quantum wires with strong Rashba spin-orbit coupling, Phys. Rev. B **66**, 073311 (2002).

[41] S.-S. Li, Y.-P. Wang, S.-J. Hu, D. Chen, C.-W. Zhang, and S.-S. Yan, Robust half-metallicity in transition metal tribromide nanowires, Nanoscale **10**, 15545 (2018).

[42] L. Hu, H. Huang, Z. Wang, W. Jiang, X. Ni, Y. Zhou, V. Zielasek, M. G. Lagally, B. Huang, and F. Liu, Ubiquitous spin-orbit coupling in a screw dislocation with high spin coherency, Phys. Rev. Lett. **121**, 066401 (2018).

[43] T. Nakamura, Y. Ohtsubo, Y. Yamashita, S.-I. Ideta, K. Tanaka, K. Yaji, A. Harasawa, S. Shin, F. Komori, R. Yukawa, K. Horiba, H. Kumigashira, and S.-I. Kimura, Giant Rashba splitting of quasi-one-dimensional surface states on Bi/InAs(110)-(2×1), Phys. Rev. B **98**, 075431 (2018).

[44] J. Han, A. Zhang, M. Chen, W. Gao, and Q. Jiang, Giant Rashba splitting in one-dimensional atomic tellurium chains, Nanoscale **12**, 10277 (2020).

[45] X. Li, B. Traoré, M. Kepenekian, L. Li, C. C. Stoumpos, P. Guo, J. Even, C. Katan, and M. G. Kanatzidis, Bismuth/silver-based two-dimensional iodide double and one-dimensional Bi perovskites: Interplay between structural and electronic dimensions, Chem. Mater. **33**, 6206 (2021).

[46] P. Hohenberg and W. Kohn, Inhomogeneous electron gas, Phys. Rev. **136**, B864 (1964).

[47] W. Kohn and L. J. Sham, Self-consistent equations including exchange and correlation effects, Phys. Rev. **140**, A1133 (1965).

[48] P. E. Blöchl, Projector augmented-wave method, Phys. Rev. B **50**, 17953 (1994).

[49] G. Kresse and J. Furthmüller, Efficient iterative schemes for *ab initio* total-energy calculations using a plane-wave basis set, Phys. Rev. B **54**, 11169 (1996).

[50] J. P. Perdew, K. Burke, and M. Ernzerhof, Generalized gradient approximation made simple, Phys. Rev. Lett. **77**, 3865 (1996).

[51] H. J. Monkhorst and J. D. Pack, Special points for Brillouin-zone integrations, Phys. Rev. B **13**, 5188 (1976).

[52] U. Herath, P. Tavadze, X. He, E. Bousquet, S. Singh, F. Muñoz, and A. H. Romero, PyProcar: A Python library for electronic structure pre/post-processing, Comput. Phys. Commun. **251**, 107080 (2020).

[53] F. Birch, Finite elastic strain of cubic crystals, Phys. Rev. **71**, 809 (1947).

[54] F. D. Murnaghan, The compressibility of media under extreme pressures, Proc. Natl. Acad. Sci. USA **30**, 244 (1944).

[55] See Supplemental Material at http://link.aps.org/supplemental/10.1103/PhysRevMaterials.8.055405 for the orbital decomposed density of states for iodine, the schematics of the Brillouin zone with high-symmetry points, the evolution of SLME with pressure, the evolution of the octahedral distortion index D with pressure, the evolution of the band structure around the Γ high-symmetry point with pressure, the bond length (Bi-I) and bond angle (Bi-I-Bi) between Bi and I at ambient pressure and 9.6 GPa, the angle between octahedra at ambient pressure and 9.6 GPa for Bi(1)-I(7/8)-Bi(2) and Bi(3)-I(17/18)-Bi(4), and the spin texture at various pressures in the *kx*-*ky* plane at the VBM around the Γ high-symmetry point, which includes Ref. [11].

[56] D. Ghosh, A. Aziz, J. A. Dawson, A. B. Walker, and M. S. Islam, Putting the squeeze on lead iodide perovskites: Pressure-induced effects to tune their structural and optoelectronic behavior, Chem. Mater. **31**, 4063 (2019).

[57] M. Gajdoš, K. Hummer, G. Kresse, J. Furthmüller, and F. Bechstedt, Linear optical properties in the projector-augmented wave methodology, Phys. Rev. B **73**, 045112 (2006).

[58] P. He, S. M. Walker, S. S.-L. Zhang, F. Y. Bruno, M. S. Bahramy, J. M. Lee, R. Ramaswamy, K. Cai, O. Heinonen, G. Vignale, F. Baumberger, and H. Yang, Observation of out-of-plane spin texture in a $SrTiO_3(111)$ two-dimensional electron gas, Phys. Rev. Lett. **120**, 266802 (2018).

[59] E. Mosconi, T. Etienne, and F. De Angelis, Rashba band splitting in organohalide lead perovskites: Bulk and surface effects, J. Phys. Chem. Lett. **8**, 2247 (2017).

[60] F. Zheng, L. Z. Tan, S. Liu, and A. M. Rappe, Rashba spin-orbit coupling enhanced carrier lifetime in $CH_3NH_3PbI_3$, Nano Lett. **15**, 7794 (2015).